The Intergranular Microstructure of Cast Mg-Zn and Mg-Zn-Rare Earth Alloys

L.Y. WEI, G.L. DUNLOP, and H. WESTENGEN

The solidification path and microstructure of cast Mg-9Zn and Mg-8Zn-1.5MM (misch metal) alloys have been investigated by a combination of thermal analysis and analytical electron microscopy. The addition of 1.5 wt pct MM had a strong influence on the as-cast microstructure with the introduction of new "ternary" interdendritic phases and structural modification of known binary phases. The temperature ranges for formation of these phases from the melt were identified, their crystal structures determined, and their compositions analyzed. Products from eutectoidal decomposition of the interdendritic phase in the binary Mg-9Zn alloy were also identified.

I. INTRODUCTION

A number of commercial magnesium alloys contain rare earth additions that apparently give improved castability and high-temperature creep resistance. However, little is known about the detailed influence on microstructure that such additions might have. This article addresses this issue for a Mg-Zn alloy containing a small addition of misch metal (MM), which is a relatively cheap source of rare earth elements for the purpose of alloying.

Previous work on Mg-Zn-RE (rare earth) systems has mainly been concerned with their phase diagrams, e.g., Mg-La-Zn,[1] Mg-Nd-Zn, and Mg-Pr-Zn.[2,3] In the present work, the microstructure of a cast Mg-Zn-MM alloy has been compared to a Mg-Zn alloy that has approximately the same Zn content in order to determine the influence of MM additions on the phase constitution and the microstructure. This article concentrates on the interdendritic phases which arise during solidification and solution treatment of these two alloys. Special attention is given to identification of the various phases and their crystal structure, morphology, and composition.

II. EXPERIMENTAL

Two alloys of the following compositions (weight percent) were gravity cast in a permanent mold: Mg-9Zn and Mg-8Zn-1.5MM. The rare earth additions were made as MM with the approximate composition (weight percent) 50Ce, 25La, 20Nd, and 3Pr. Measurement of solidification curves was carried out separately on both alloys during solidification at a cooling rate of ~1 °C/s.

The as-cast alloys were heat-treated at 315 °C for 4 hours followed by a water quench. This treatment corresponds to a solution treatment prior to age hardening.

Specimens for optical metallography were mechanically polished using standard techniques and subsequently etched in $1/3HNO_3$ in ethanol. These specimens were also studied by scanning electron microscopy (SEM) in a JEOL* 733 scanning electron microscope. The average size of the dendrite cells in the cast alloys was measured by the linear intersect method, and the volume fraction of the intermetallic phases was obtained by point counting on polished surfaces using optical microscopy. Thin foils for transmission electron microscopy (TEM) were prepared by jet electropolishing in $1/3HNO_3$ in ethanol at 8 to 15 V and ~0 °C. The thin foils were subjected to a short ion beam thinning operation of about 1 hour with an incidence angle of ~15 deg. This removed the oxide layers which formed on the foil surfaces during electropolishing. The specimens were examined in a JEOL 2000FX transmission electron microscope/scanning transmission electron microscope (TEM/STEM) instrument with an attached Link AN 10000 energy-dispersive X-ray (EDX) system. Microanalyses using the EDX system were made quantitative using the Link RTS-2/FLS computer program which compares spectra against standard peak profiles, applies the thin foil approximation, and makes corrections for absorbtion.[4,5] Foil thicknesses were established using the two-beam convergent beam electron diffraction technique.[6] The K_{xsi} value for Mg was determined by measurements on an olivine standard mineral sample. Standard peak profiles were obtained from pure samples of Mg, Zn, La_2O_3, CeO_2, and Nd_2O_3. The camera length for electron diffraction patterns obtained from the specimens was determined from sharp diffraction rings on the diffraction patterns originating from a thin film of MgO on the foil surfaces. The estimated error limit for measurements on the diffraction patterns was about ±0.05 mm, leading to a relative error for the lattice parameters of about ±1 to 1.5 pct.

*JEOL is a trademark of Japan Electron Optics Ltd., Tokyo, Japan.

III. RESULTS

A. *Thermal Analysis*

The differential cooling curves in Figure 1 show inflections that appear as peaks on the dT/dt (T = temperature and t = time) curves. These peaks can be expected to correspond to the formation of solid phases during cooling.

L.Y. WEI, Senior Research Scientist, is with the Department of Engineering Materials, Luleå University of Technology, S 971 87 Luleå, Sweden. G.L. DUNLOP, Professor and Director of CRC for Alloy and Solidification Technology (CAST), is with the Department of Mining and Metallurgical Engineering, The University of Queensland, Q 4072, Australia. H. WESTENGEN, Section Manager, is with Magnesium Materials Technology, Norsk Hydro a.s, Research Centre Porsgrunn, N-3901 Porsgrunn, Norway.

Manuscript submitted August 17, 1994.

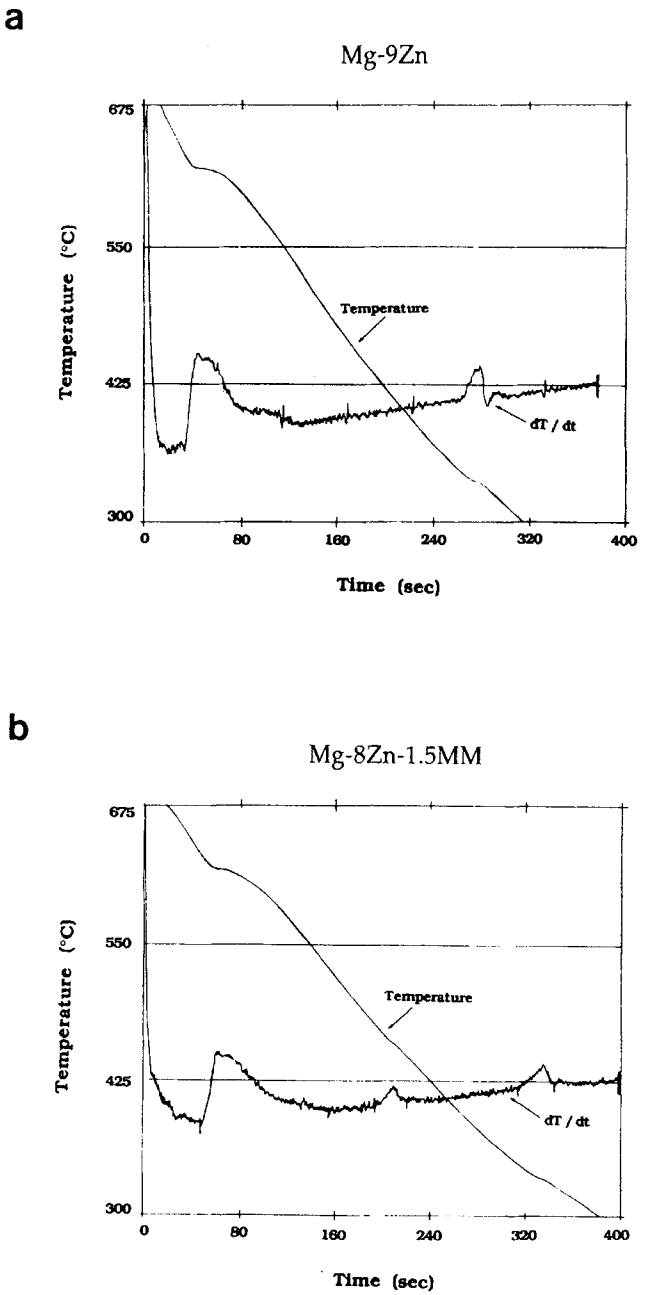

Fig. 1—Cooling curves obtained during solidification of (*a*) Mg-9Zn and (*b*) Mg-8Zn-1.5MM alloys.

Table I. Reaction Temperature Ranges (°C) for Exothermic Reactions during Solidification of Mg-9Zn and Mg-8Zn-1.5MM Alloys

	$L \rightarrow \alpha$ (Mg)		Peak 2		Peak 3	
Reaction	Onset	Finish	Onset	Finish	Onset	Finish
Mg-9Zn	632	522	—	—	340	317
Mg-8Zn-1.5MM	625	523	480	447	346	316

The temperature ranges for these solidification reactions are given in Table I. The first of these inflections (in the approximate range 632 °C to 522 °C) is due to the formation of the primary α-Mg solid solution dendrites. Both alloys also showed inflections in the approximate range 346 °C to 316 °C, and the alloy containing rare earth additions showed an additional reaction between 480 °C and 447 °C. An obvious endothermal peak also occurred in the range 325 °C to 317 °C in the *dT/dt* curve of the Mg-9Zn alloy.

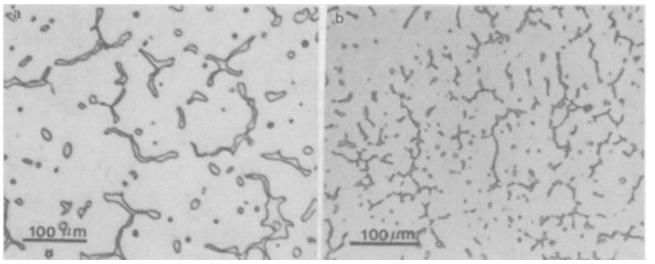

Fig. 2—Optical micrographs for the as-cast alloys: (*a*) Mg-9Zn and (*b*) Mg-8Zn-1.5MM.

Table II. Average Dendrite Sizes (Linear Intercept) and Volume Fractions of the Intergranular Phases

	Dendrite Size (μm)		Volume Fraction of
Alloy	Range	Average	Intergranular Phases
Mg-9Zn	30 to 270	98	12.9 ± 1.7 pct
Mg-8Zn-1.5MM	15 to 88	41	21.3 ± 1.5 pct

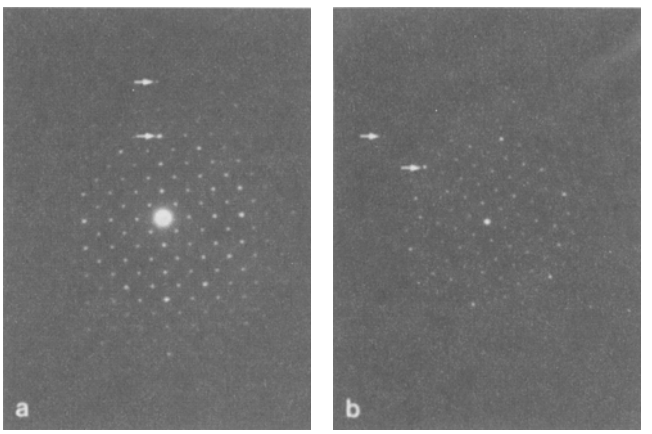

Fig. 3—SAED patterns from coarse interdendritic precipitates in the cast Mg-9Zn alloy: (*a*) [010] zone axis and (*b*) [111] zone axis.

B. *General Microstructure of the Cast Alloys*

Optical micrographs of the cast alloys are shown in Figure 2. Both alloys had typical dendritic solidification microstructures with significant amounts of interdendritic phases formed by the divorced eutectic reaction. The microstructure of the Mg-Zn alloy was significantly coarser than the Mg-Zn-MM alloy, but the volume fraction of the intergranular phases in the Mg-9Zn alloy was less than for the Mg-8Zn-1.5MM alloy. This is shown clearly by the measurements of average dendrite sizes and the volume fractions of intergranular phases shown in Table II.

C. *Intergranular Phases in the As-Cast Mg-9Zn Alloy*

Selected area electron diffraction (SAED) (Figure 3) showed that the coarse interdendritic precipitates visible in Figure 2(a) were predominantly the $Mg_{51}Zn_{20}$ phase.[7] The crystal lattice of this phase is orthorhombic, space group *Immm*, with a = 1.4083 nm, b = 1.4486 nm, and c =

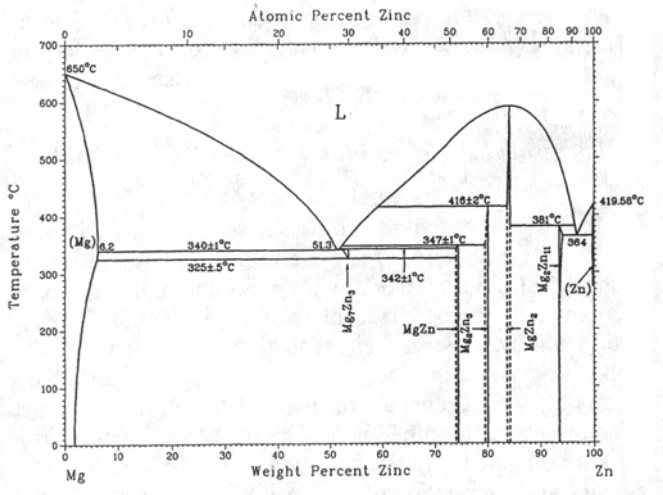

Fig. 4—Phase diagram of the Mg-Zn binary system.[8]

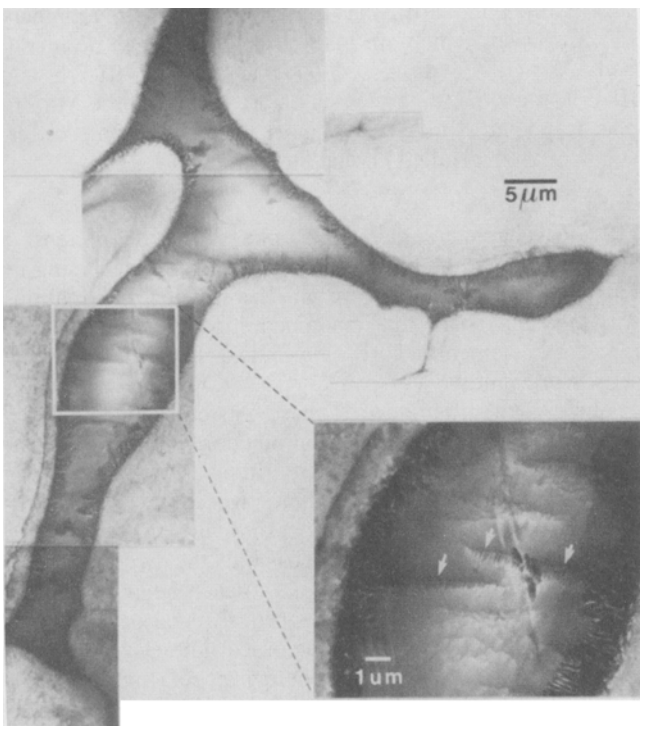

Fig. 5—Early stage of eutectoidal decomposition of $Mg_{51}Zn_{20}$ interdendritic phase.

1.4025 nm. Higashi et al.[7] indicated that the crystal structure of $Mg_{51}Zn_{20}$ can be described as an arrangement of icosahedral coordination polyhedra. The intense diffraction spots marked with arrows in Figures 3(a) and (b) display the twofold and threefold symmetry of the icosahedra which have 5-3-2 diffraction symmetry. Inspection of the phase diagram in Figure 4[8] suggests that the predominant $Mg_{51}Zn_{20}$ interdendritic phase corresponds to the Mg_7Zn_3 phase that forms as a result of the eutectic reaction.

It was sometimes found that some smaller precipitates existed within the coarse $Mg_{51}Zn_{20}$ eutectic phase. Selected area electron diffraction indicated that this type of phase had the same crystal structure as the $MgZn_2$ Laves phase.[9] The three micrographs in Figures 5 and 6 show interdendritic regions with different morphologies from the same

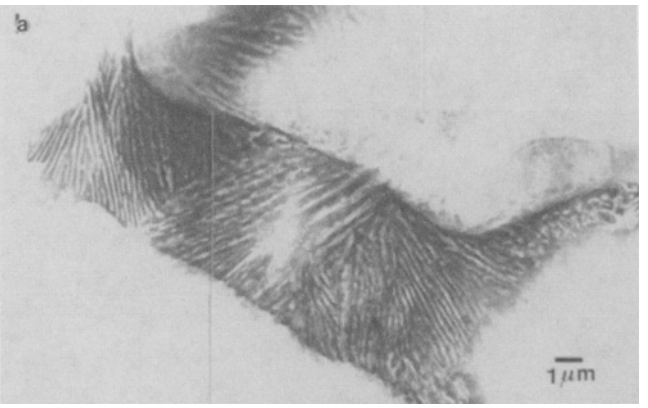

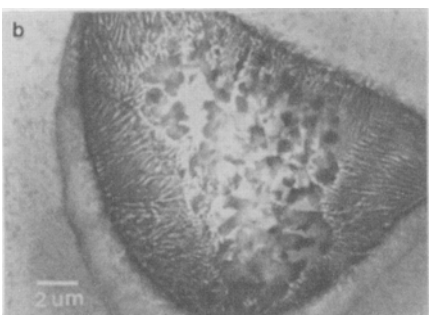

Fig. 6—TEM micrographs of the eutectoidal decomposition of the $Mg_{51}Zn_{20}$ interdendritic phase in as-cast Mg-9Zn during cooling after solidification. (*a*) Complete eutectoidal decomposition of the $Mg_{51}Zn_{20}$ phase to α(Mg) and MgZn. (*b*) Decomposition of the $Mg_{51}Zn_{20}$ phase to a lamellar product of α(Mg) and MgZn at the outer part of an interdendritic particle and to α(Mg) and $MgZn_2$ Laves phases in the interior.

as-cast specimen of the Mg-9Zn alloy. From these micrographs, it is clear that the $Mg_{51}Zn_{20}$ phase had partially decomposed during cooling after solidification. An early stage in this eutectoid decomposition is illustrated in Figure 5. Here, the outermost part of the precipitate has decomposed to a lamellar eutectoid product according to the reaction

$$Mg_{51}Zn_{20} \rightarrow \alpha(Mg) + MgZn$$

As indicated by the arrows in Figure 5, this lamellar decomposition product extended well into the interior of the intergranular precipitates, where it apparently nucleated on dislocations. Figure 6(a) shows a particle that had decomposed completely. Analysis by scanning transmission electron microscopy/energy dispersive X-ray (STEM/EDX) showed that the composition of the MgZn phase was (weight percent) 25.7 ± 1.3 Mg and 74.3 ± 1.3Zn, which corresponds with the value of Mg-74.5 wt pct Zn given by Clark and Rhines[10] for virtually stoichiometric MgZn. The crystal structure of this phase has yet to be determined.

Another type of decomposition product is shown in Figure 6(b). Here, as previously, the outer part of the particle decomposed to the lamellar eutectoidal mixture of α(Mg) + MgZn, but the interior of the grain contained granular precipitates with the same crystal structure of the $MgZn_2$ Laves phase. The chemical composition of these granular precipitates was determined to be (weight percent) 22.3 ± 0.4 Mg and 77.7 ± 0.4 Zn. This corresponds to a stoichiometry of $MgZn_{1.3}$.

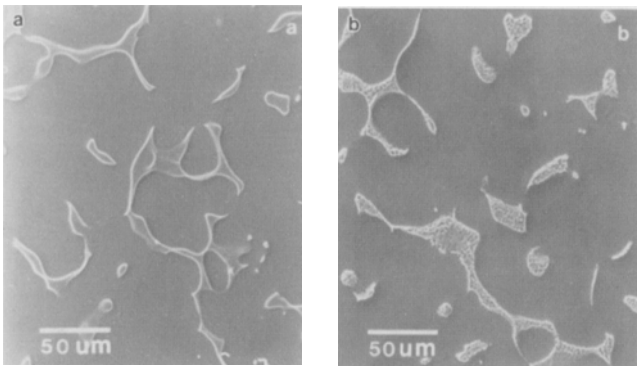

Fig. 7—SEM micrographs of the Mg-9Zn alloy: (*a*) as cast and (*b*) after solution treatment at 315 °C for 4 hours.

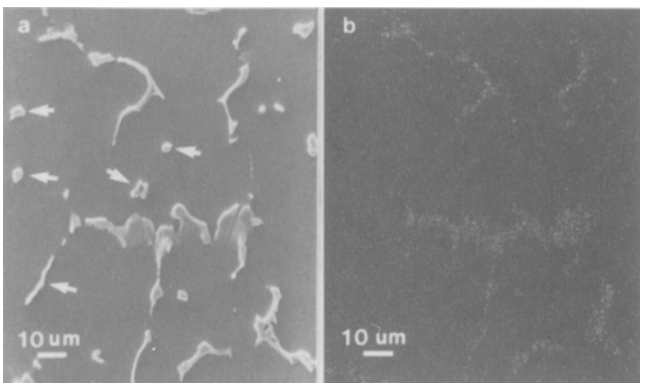

Fig. 8—(*a*) SEM micrograph from the as-cast Mg-8Zn-1.5MM alloy; particles marked by arrows are the pseudobinary Mg-Zn phases. (*b*) Ce map of the same field, obtained by wavelength X-ray spectrometry.

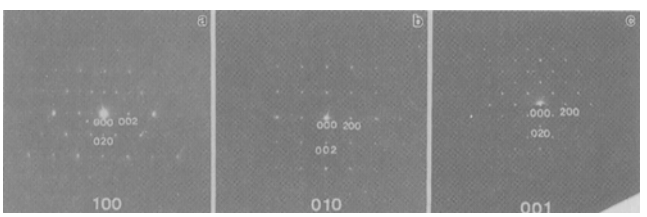

Fig. 9—Low-index SAED patterns taken from *T* phase in Mg-8Zn-1.5MM alloy: (*a*) [100] zone axis, (*b*) [010] zone axis, and (*c*) [001] zone axis.

The rim around the intergranular precipitates in Figures 5 and 6(a) and (b) was α(Mg), which probably formed during formation of the divorced eutectic structure. The spotty dark contrast in the α(Mg) in these micrographs is due to radiation damage arising from ion milling.

D. *Intergranular Phases in Mg-9Zn Alloy after Solution Treatment*

As can be seen from Figure 4, the eutectoid temperature for binary Mg-Zn alloys is approximately 325 °C. A solution treatment temperature of 315 °C was therefore chosen for subsequent studies of the age-hardening behavior of these alloys. Changes of morphology which occurred in the intergranular phases during a 4-hour solution treatment at 315 °C followed by a water quench are revealed in the SEM micrographs shown in Figure 7. All of the $Mg_{51}Zn_{20}$ particles decomposed completely to form an intimate mixture of an intermetallic phase interwoven with α(Mg). The intermetallic phase was subsequently shown to have a crystal structure consistent with $MgZn_2$ Laves phase.

E. *Intergranular Phases in the As-Cast Mg-8Zn-1.5MM Alloy*

Three types of interdendritic phases were identified in the cast Mg-8Zn-1.5MM alloy, and these could not be distinguished from each other by their morphologies. The most predominant interdendritic phase was a ''ternary'' phase with a high rare earth content that here is called *T* phase. This phase has been observed in some previous work[11] but was not properly characterized then; therefore, its crystal structure was determined here. The other two interdendritic phases contained only small amounts of the rare earth elements and were virtually binary Mg-Zn phases. Figure 8(a) is a SEM micrograph taken from the as-cast Mg-8Zn-1.5MM alloy. With the Ce X-ray map of the same field, shown in Figure 8(b), the *T* phase and the pseudobinary Mg-Zn phases which are marked by arrows can be identified. As will be discussed later in sections III-E-2 and III-E-3, the two ''binary'' phases are related to the Mg_4Zn_7 phase and the $MgZn_2$ Laves phase but with some differences in their detailed crystal structures.

1. *T phase*

Initial characterization of *T* phase required extensive electron diffraction, but later it could be identified using its EDX spectrum as a ''fingerprint,'' as it was found that this was the only phase that contained substantial amounts of rare earth elements. Three low-index SAED patterns are shown in Figure 9.

The crystal structure of *T* phase was determined using a procedure involving geometric projection of diffraction patterns taken from a systematic tilting series.[12] In this method, the crystal is tilted about two closely packed reciprocal lattice directions in order to obtain a series of low-index diffraction patterns. If possible, the two reciprocal directions should be perpendicular to each other in order to obtain a highly symmetrical reciprocal plane of the investigated crystal. The shortest reciprocal lattice vector from each diffraction pattern was then projected onto a plane which was perpendicular to the tilt axis. The projected reciprocal lattice vectors then provided two planes in the reciprocal lattice and so enabled determination of the reciprocal unit cell and, as a consequence, the crystal lattice unit cell. From this analysis, it was found that *T* phase has a *c*-centered orthorhombic crystal structure with lattice parameters $a = 0.96$ nm, $b = 1.12$ nm, and $c = 0.94$ nm. This structure determination was tested for a number of *T*-phase precipitates, and in each case, the results were found to be consistent.

Microanalysis of *T* phase by STEM/EDX gave the following composition (weight percent): 25.8 ± 2.1 Mg; 51.7 ± 1.9 Zn; 8.0 ± 0.6 La; 11.3 ± 1.0 Ce; 3.2 ± 1.0 Nd, corresponding to the atomic composition $Mg_{52.6}Zn_{39.5}MM_{7.9}$ or $(Mg,Zn)_{92.1}MM_{7.9}$. The error limits given in these analyses correspond to the standard deviation between measurements on a number of different precipitates.

Further microanalysis by STEM/EDX using an ultrathin window indicated that a small amount of oxygen might be present in *T* phase (spectrum in Figure 10). Spectra taken

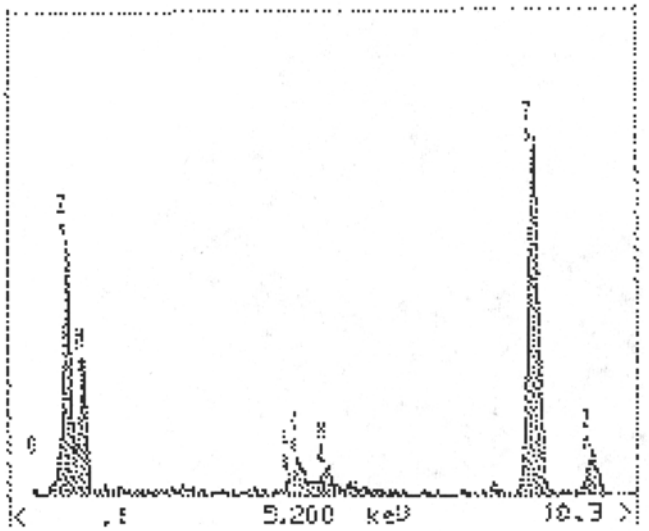

Fig. 10—STEM/EDX spectra from the T phase in the as-cast Mg-8Zn-1.5MM alloy using an ultrathin window. Note the small peak arising from oxygen.

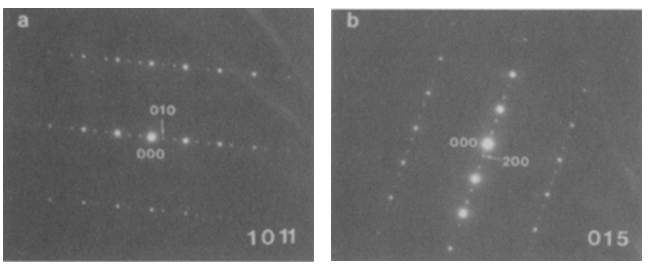

Fig. 11—SAED patterns from an Mg_4Zn_7 interdendritic precipitate (*a*) [1011] zone axis and (*b*) [015] zone axis.

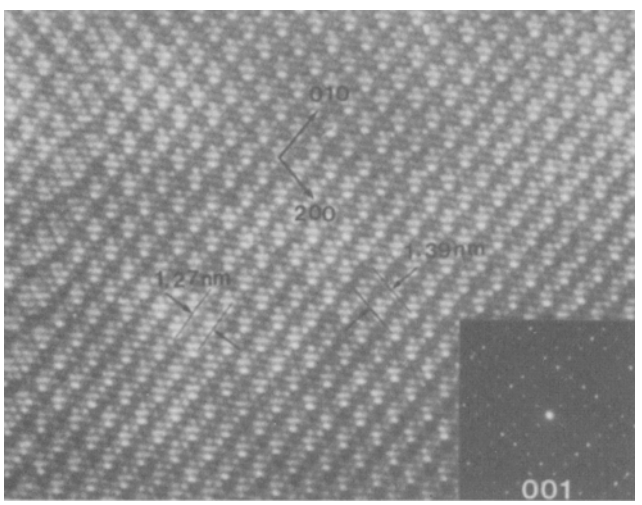

Fig. 12—HREM image of the projected (001) plane of Mg_4Zn_7 phase in the Mg-8Zn-1.5MM alloy.

under similar conditions from both the matrix and Laves phase did not contain any discernible peak that could be attributed to oxygen. It is therefore considered that the oxygen peak in Figure 10 probably did not arise from a surface oxide film but was due to oxygen dissolved within the bulk of T phase. These results were supported by scanning

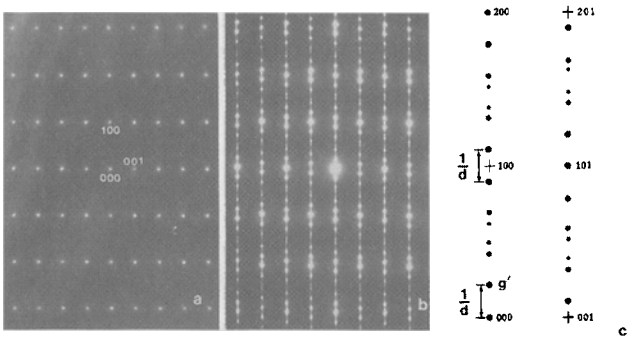

Fig. 13—[010] zone axis SAED patterns of Laves phase (*a*) Mg-9Zn alloy and (*b*) Mg-8Zn-1.5MM alloy. (*c*) Schematic solution of the diffraction pattern in (b), ":" represents the splitting position corresponding to some deflection from the basic $MgZn_2$ structure.

Auger microanalysis on the various phases after substantial sputtering with argon ions to remove the oxide film.

2. *Mg_4Zn_7 Phase*

Mg_4Zn_7 has a B-centered monoclinic $B2/m$ crystal structure with lattice parameters[13] $a = 2.596$ nm, $b = 1.428$ nm, $c = 0.524$ nm, and $\gamma = 102.5$ deg. The number of Mg_4Zn_7 formula units per unit cell is 10. Typical SAED patterns from an Mg_4Zn_7 interdendritic precipitate are shown in Figure 11. Of particular interest in these diffraction patterns is the 3×3 variation in intensity of diffraction spots which suggests the existence of long-range ordering structure with periodicity in [200] and [010] directions. The high-resolution micrograph in Figure 12 taken with an [001] beam direction shows the two-dimensional crystal structure in an (001) crystal plane. From this image, it seems that there is a change in stacking sequence which takes place at every third atomic layer in both the [200] and [010] directions. The structure is complicated as evidenced by the variation of intensities of reflections in the associated 001 diffraction pattern. No rare earth elements were detected by STEM/EDX microanalysis of the Mg_4Zn_7 phase.

3. *$MgZn_2$ Laves Phase*

Comparison of the two [010] SAED patterns obtained from precipitates in Mg-Zn and Mg-Zn-MM alloys (Figure 13) shows that some of the coarse interdendritic precipitates in the Mg-Zn-MM alloy had a crystal structure that was similar to the $MgZn_2$ Laves phase. The diffraction patterns from this phase, however, were considerably more complicated than for the binary Mg-Zn alloy. The diffraction pattern in Figure 13(b) shows a systematic splitting of alternate reflections from the basic $MgZn_2$ structure. In addition, a number of extra reflections are present along the (100) direction. The details of the diffraction pattern are best understood from the schematic diagram in Figure 13(c). The diffraction features suggest that the crystal structure of the Laves phase in the Mg-Zn-MM alloy is modulated by planar translation interfaces which are equivalent to a uniform sequence of antiphase boundaries (APBs) in a long-period superstructure.[14] From the splitting distance of the superlattice spots, the mean half-period, which is measured in units of (100) interplanar spacings, is $M \approx 4.86$. The displacement vector $\mathbf{R}$ for the APBs can be calculated from the systematic splitting of reflections. As shown by Van Dyck et al.,[15] the superstructure reflections (or the satellites

Table III. Systematic Splitting Condition for Reflections in [010] Electron Diffraction Patterns from $MgZn_2$ Laves Phase in Mg-8Zn-1.5MM Alloy

Diffraction	$h00$	$00l$	$h0l$
Splitting condition	$h = 2n + 1$	$l = 2n + 1$	$h + l = 2n + 1$

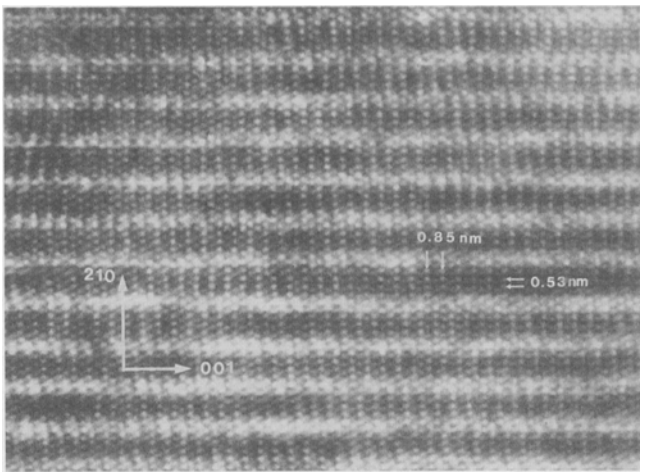

Fig. 14—HREM image of projected (010) plane of Laves phase in the Mg-8Zn-1.5MM alloy.

of the basic spots) of a periodic APB structure are peaked at positions given by

$$\mathbf{g}' = g - (1/d)(m - \mathbf{g}\cdot\mathbf{R}) \qquad [1]$$

where $\mathbf{g}'$ and $\mathbf{g}$ are the diffraction vectors of the superstructure and the basic lattice, respectively, m is an integer, d is the repeat distance or half-period of the APB structure, and $\mathbf{R}$ is the displacement vector of the interfaces. The splitting of the basic reflections means $\mathbf{g}\cdot\mathbf{R} \neq$ integer; otherwise, $\mathbf{g}\cdot\mathbf{R}$ = integer. From the systematic splitting condition in the [010] SAED (Figure 13), summarized in Table III, the displacement at each APB can then be deduced to be $\mathbf{R}$ = [1/201/2].

It is thus concluded that the Laves phase in Mg-Zn-MM alloys has a translation interface modulated structure in which periodic APBs have been introduced perpendicular to the (010) plane. The mean half-period is $M \approx 4.86$, and the displacement vector at the APBs is [1/201/2].

The high-resolution electron microscopy (HREM) image of projected (010) planes shown in Figure 14 reveals the antiphase domain structure with alternate contrast every five lattice spacings in the [210] direction. This is consistent with the results obtained by selected area diffraction.

Microanalysis by STEM/EDX showed that the $MgZn_2$ Laves phase in the Mg-Zn-MM alloy contained (weight percent) 20.2 ± 2.8 Mg, 78.2 ± 2.8 Zn, 0.4 ± 0.1 Ce, and 1.2 ± 0.4 Nd. No La was detected in the structure.

F. *Precipitation during Solution Treatment of the Mg-8Zn-1.5MM Alloy*

None of the three intergranular phases which were present after solidification of the Mg-8Zn-1.5MM alloy decomposed during solution treatment at 315 °C. Instead, a fourth phase (B phase) was found to precipitate in the vicinity of the T-phase precipitates. As shown in Figure 15(a), the B-phase precipitates formed with either a rodlike morphology or as a rim on the existing T-phase particles. B phase also formed along the grain boundaries (Figure 15(b)).

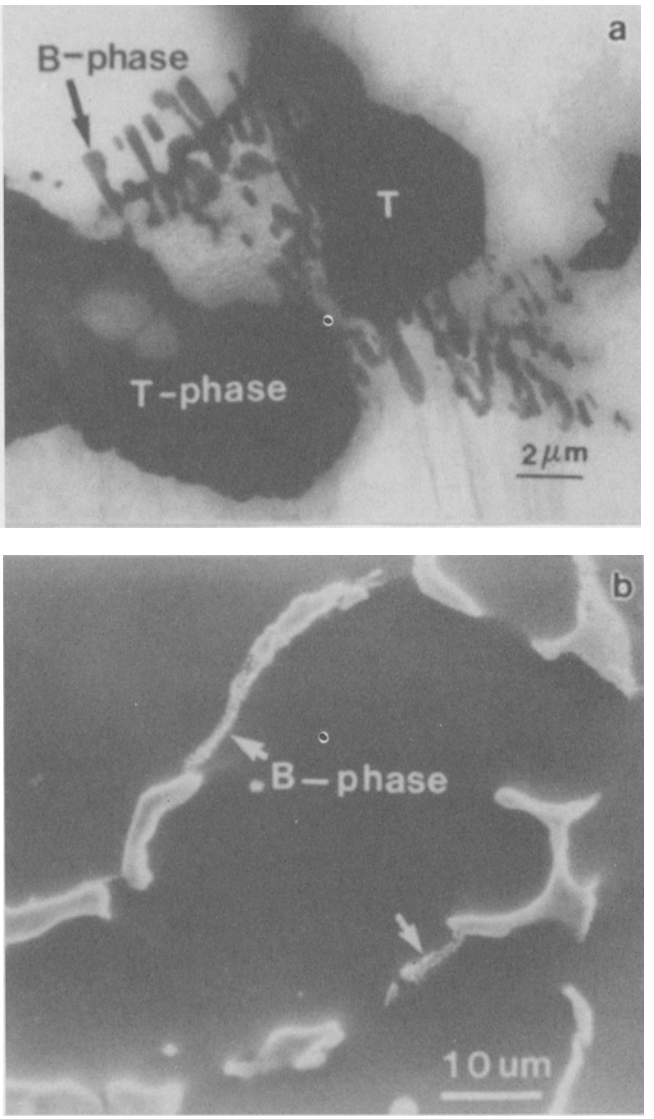

Fig. 15—Formation of B phase during heat treatment of the Mg-8Zn-1.5MM alloy at 315 °C: (*a*) rodlike B-phase precipitates in vicinity of T phase (TEM) and (*b*) B phase at grain boundaries (SEM).

Selected area electron diffraction indicated that the crystal structure of B phase is not consistent with either $MgZn_2$ Laves phase or the Mg_2Zn_3 triclinic phase, which is reported to have a = 1.724 nm, b = 1.445 nm, c = 0.520 nm, α = 96 deg, β = 89 deg, and γ = 138 deg.[9] The crystal structure of B phase was determined using the same method of geometric projection of diffraction patterns described in Section III–E–1. This showed that B phase indeed has a triclinic Bravais lattice but with the following lattice parameters: a = 0.87 nm, b = 1.20 nm, c = 1.40 nm, α = 107 deg, β = 91, and γ = 110 deg.

As shown in the lattice image of Figure 16 and the associated diffraction pattern, the structure of B phase was severely modulated. This modulation was most extensive in the center of the precipitates and decreased toward their edge, where a more uniform structure was generally noted.

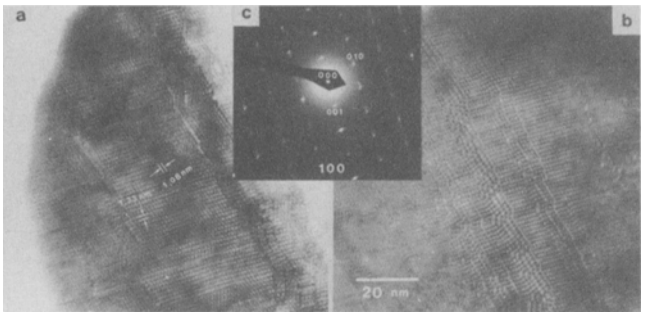

Fig. 16—Lattice image of projected (100) plane of *B* phase in the Mg-8Zn-1.5MM alloy: (*a*) an outermost area of a particle, (*b*) the interior of the same particle, and (*c*) [100] zone axis SAED pattern from the particle shown in (a) and (b).

Analysis by STEM/EDX gave an average composition for *B* phase (weight percent) of 44.9 ± 4.2 Mg, 52.7 ± 4.2 Zn, 1.6 ± 0.6 Nd, and 0.8 ± 0.3 Ce, which is equivalent to (atomic percent) $Mg_{69.1}Zn_{30.3}RE_{0.6}$. This is close to the composition of the previously discussed $Mg_{51}Zn_{20}$ phase that was found in the binary Mg-Zn alloy, but as noted here, their crystal structures are very different.

IV. DISCUSSION

A. *The Solidification Path and Interdendritic Phases in the Mg-9Zn Alloy*

The solid phases that form during the solidification process can be deduced from the experimental results obtained by thermal analysis, TEM, and STEM/EDX. In the Mg-9Zn alloy, most of the reaction $L \rightarrow L + \alpha(Mg)$ occurred in the temperature range 632 °C to 522 °C. The next inflection in the cooling curve occurred between 340 °C and 317 °C, corresponding to the formation of the $Mg_{51}Zn_{20}$ phase, which is consistent with the eutectic product Mg_7Zn_3 that is usually shown in Mg-Zn binary phase diagrams (Figure 4). The TEM observations described in Section III–C indicated that $Mg_{51}Zn_{20}$ was a thermally unstable phase and decomposed at lower temperatures. This decomposition is possibly associated with the small endothermal reaction peak in the range 325 °C to 317 °C on the *dT/dt* curve in Figure 1(a).

B. *Eutectoidal Decomposition of $Mg_{51}Zn_{20}$ in the Mg-9Zn Alloy*

The eutectoidal decomposition of Mg_7Zn_3 phase in Mg-Zn alloys has previously been investigated by metallographic examination, X-ray diffraction, and dilatometry. Clark and Rhines[10] reported that in the Mg-Zn system with Zn contents ranging from 0 to 85 wt pct, the Mg_7Zn_3 phase decomposed eutectoidally to magnesium solid solution and MgZn (with 74.5 wt pct Zn) at temperatures below 325 °C. The MgZn phase was found to be stable over the temperature range 315 °C to 93 °C. Kitchingman and Vesey[16] reported that the eutectoid decomposition product was $\alpha(Mg) + MgZn$ above 200 °C, and below this temperature, the decomposition product was $\alpha(Mg) + MgZn_2$.

In the present work, the eutectoid decomposition of interdendritic $Mg_{51}Zn_{20}$ was clearly revealed by TEM and SEM. The decomposition reaction occurred mainly in the temperature range 325 °C to 317 °C. The lamellar eutectoid $\alpha(Mg) + MgZn$ occurred at the early stage of decomposition and nucleated on phase boundaries between the Mg matrix and the $Mg_{51}Zn_{20}$ phase and then extended into the interior of the $Mg_{51}Zn_{20}$ particles. Granular precipitation of $MgZn_2$ and $\alpha(Mg)$ occurred in the interior of the $Mg_{51}Zn_{20}$ particles. The $Mg_{51}Zn_{20}$ phase completely decomposed during heat treatment at 315 °C, and the terminal decomposition products were $MgZn_2$ Laves phase and $\alpha(Mg)$. It has been shown elsewhere that $MgZn_2$ is stable during long-term aging at 200 °C.[17] Therefore, it can be concluded that MgZn is not stable below 315 °C, whereas $MgZn_2$ is an equilibrium phase and is stable between 315 °C and room temperature.

Two different eutectoid temperatures have been reported for the binary Mg-Zn system. Clark and Rhines[10] and Clark et al.[8] (Figure 4) give the eutectoid temperature as 325 °C, while the phase diagram attributed to Park reported the eutectoid temperature to be at 312 °C.[18,19] Since the eutectoid decomposition in the present work was found to be complete at about 315 °C, it would seem that the eutectoid temperature reported by Clark and Rhine and Clark et al. is more correct.

C. *The Effect of Misch Metal Additions on the Microstructure*

Two Mg-Zn phases, Mg_4Zn_7 and the modified $MgZn_2$ (containing 1.0 wt pct Nd and 0.5 wt pct Ce), formed in the rare earth containing alloy in a temperature range corresponding to peak 3 in Figure 1(b) (346 °C to 316 °C). This temperature range was similar to that in which intermetallic precipitates formed in the binary Mg-9Zn alloy. During heat treatment at 315 °C, B phase also formed from the supersaturated $\alpha(Mg)$ solid solution. Comparison of the cooling curve of the ternary alloy with that of the binary Mg-9Zn alloy indicates that the inflection between 480 °C to 447 °C results from the MM addition and that the *T* phase probably formed in this temperature range.

The small addition (1.5 wt pct) of MM had a considerable effect on the phase constitution and microstructure of the Mg-Zn-MM alloy. The significantly finer microstructure of the Mg-Zn-MM alloy indicates that the addition of MM can decrease the growth of dendritic crystals and effectively reduce the size of intergranular particles. The formation of the ternary phase (*T* phase), which is the predominant intergranular phase and which forms at a temperature about 100 °C higher than for the eutectic phases in Mg-Zn alloys, is probably the main cause for this refinement in microstructure. Growth of the dendrites would have slowed significantly at about 480 °C when the eutectic *T* phase formed between the dendrite arms. The total amount of interdendritic phases was increased by the rare earth addition.

D. *Modulation of Crystal Structures Due to Rare Earth Additions*

The long-period antiphase domain structure of $MgZn_2$ Laves phase containing about 1.2 pct Nd and 0.4 pct Ce indicates that the small amount of rare earth elements contained in this phase had a strong influence on its crystal structure. It is believed that one of the main factors contributing to the existence of Laves phases is a geometrical

Table IV. Proportion of Various Rare Earth Elements in Intermetallic Phases (Weight Percent)

	La	Ce	Nd	Pr
MM	26	51	20	3
T phase	36	51	13	0
Laves $MgZn_2$ phase	0	25	75	0
B phase	0	33	67	0

Table V. Atomic Radii of Mg and Rare Earth Elements

Element	Mg	Nd	Ce	Pr	La
Atomic radii (Å)	1.770	2.013	2.017	2.020	2.077

size factor. For the AB_2 Laves phase, the A atoms must be larger than B atoms and they must be able to contract or expand to achieve the ideal ratio of $R_A/R_B = 1.225$.[20] The differences in atomic radii between magnesium (1.770 Å), neodymium (2.013 Å), and cerium (2.017 Å) could be one of the main causes of the periodic antiphase domain structure in Laves phase in the Mg-Zn-MM alloy. Although the atomic arrangement for the rare earth elements in Laves phase is still unknown, it can be expected that some magnesium atoms are replaced by the rare earth elements. The strain caused by the atomic size difference could be relieved by the formation of antiphase domains at regular intervals provided that the antiphase boundary energy is not large.

Calculation of lattice parameters from SAED and with MgO diffraction rings to provide a standard for the camera length showed that the lattice parameters of the Laves phase in the ternary alloy were $a = 0.53$ nm and $c = 0.85$ nm. Compared with the lattice parameters of $MgZn_2$ Laves phase reported in the literature ($a = 0.518$ nm and $c = 0.852$ nm, and $a = 0.5221$ nm and $c = 0.8567$ nm),[9] there is a slight increase of the (100) interplanar spacing, indicating that the relaxation due to the APB structure also results in a change of lattice parameter.

The nonintegral value of the antiphase domain half-period, *M*, can be interpreted by considering a mixture of domains of different integral values of *M*. As described by Cowley,[21] the structural modulations are locally commensurate but statistically incommensurate.

E. *The Proportion of the Various Rare Earth Elements in the Intermetallic Phases*

Data obtained from the comparison between the composition of MM and the proportions of different rare earth elements in various phases of the Mg-Zn-MM alloy are shown in Table IV.

According to the atomic radii, shown in Table V, the sequence of declining solubility of various rare earth elements in α(Mg) can be expected to be neodymium, cerium, praseodymium, and lanthanum.

Most of the La in the alloy was dissolved in the *T* phase which formed at higher temperatures. By way of contrast, the modified Laves phase which formed at lower temperatures had a relatively high content of Nd and an indiscernible amount of La. This suggests that the large size of the La atoms made it more difficult for them to be dissolved in Mg solid solution than Nd and Ce.

V. CONCLUSIONS

1. Addition of 1.5 wt pct MM has a strong influence on the microstructure of a cast Mg-8Zn alloy.
2. The main interdendritic phase which formed during solidification of the binary Mg-9Zn alloy is the $Mg_{51}Zn_{20}$ eutectic phase.
3. *T* phase formed in the temperature range 480 °C to 447 °C during solidification of the Mg-8Zn-1.5MM alloy. The Bravais lattice of *T* phase was determined to be *C*-centered orthorhombic with the lattice parameters $a = 0.96$ nm, $b = 1.12$ nm, and $c = 0.94$ nm. The composition was determined to be (weight percent) 25.8 ± 2.1 Mg, 51.7 ± 1.9 Zn; 8.0 ± 0.6 La, 11.3 ± 1.0 Ce, and 3.2 ± 1.0 Nd.
4. Mg_4Zn_7 and $MgZn_2$ Laves phases formed in the temperature range 346 °C to 316 °C during solidification of the Mg-8Zn-1.5MM alloy.
5. The $MgZn_2$ Laves phase in the Mg-Zn-MM alloy has an interface modulated structure. The APBs are perpendicular to the [210] direction; the mean half-period, or the domain size, is $M = 4.86$, and the displacement vector of the APB is [1/201/2]. STEM/EDX revealed that about 1.2 pct Nd and 0.4 pct Ce was present in this phase.
6. The Mg_4Zn_7 phase in the Mg-Zn-MM alloy has a (3 × 3) long-period structure.
7. The eutectic $Mg_{51}Zn_{20}$ phase in Mg-9Zn alloy decomposed at temperatures between 325 °C and 317 °C. The products of this eutectoid decomposition were lamellar MgZn, granular $MgZn_2$, and α(Mg). MgZn formed at an early stage of the decomposition, and the terminal products of decomposition were $MgZn_2$ and α(Mg).
8. The *T* phase in the Mg-8Zn-1.5MM alloy is thermally stable at temperatures below 315 °C. The *B* phase was found to be formed from supersaturated solid solution during heat treatment at 315 °C. The *B* phase has a triclinic crystal lattice of $a = 0.87$ nm, $b = 1.20$ nm, $c = 1.40$ nm, $\alpha = 107$ deg, $\beta = 91$ deg, and $\gamma = 110$ deg. Its composition is 44.9 ± 4.2 Mg, 52.7 ± 4.2 Zn, 1.6 ± 0.6 Nd, and 0.8 ± 0.3 Ce.

ACKNOWLEDGMENTS

The experimental work was carried out at Chalmers Technical University, Sweden. Financial support from the Swedish Board for Technical Development and Norsk Hydro a.s is gratefully acknowledged. Assistance from C.H. Li with the SEM and discussions with P. Liu are gratefully acknowledged.

REFERENCES

1. T.V. Dobatkina, E.V. Muratova, and E.I. Drozdova: *IZV. Akad. Nauk. SSSR Met.*, 1987, vol. 1, pp. 205-08.
2. M.E. Drits, E.M. Padezhnova, and N.V. Miklina: *IZV. Akad. Nauk. SSSR Met.*, 1974, vol. 3, pp. 225-28.
3. V.V. Kinzhrbalo, A.T. Tivanchuk, and E.V. Mel'nik: in *Stable and Metastable Phase Equilibria in Metallic Systems*, M.E. Drits, ed., Nauka, Moscow, 1986, pp. 70-79.
4. J.I. Goldstein, J.L. Costley, G.W. Lorimer, and S.J.B. Reed: *Scanning Electron Microscopy/1977*, O. Johari, ed., IITRI, Chicago, IL, 1977, vol. 1, pp. 315-24.
5. J.I. Goldstein: in *Introduction to Analytical Electron Microscopy*, J.J. Hren, J.I. Goldstein, and D.C. Joy, eds., Plenum Press, New York, NY, 1979, pp. 83-120.

6. P.M. Kelly, A. Jostsons, R.G. Blake, and J.G. Napier: *Phys. Status Solidi A*, 1975, 31, pp. 771-80.
7. I. Higashi, N. Shiotani, M. Uda, T. Mizoguchi, and H. Katoh: *J. Solid State Chem.*, 1981, vol. 36, pp. 225-33.
8. J.B. Clark, L. Zabdyr, and Z. Moser: *Binary Alloy Phase Diagrams*, 2nd ed., T.B. Massalski, H. Okamoto, P.R. Subramanian and L.' Kacprzak, eds., ASM INTERNATIONAL, Materials Park, OH, 1990, pp. 2571-72.
9. W.B. Pearson: in *Pearson's Handbook of Crystallographic Data for Intermetallic Phases*, P. Villars and L.O. Calvert, eds., ASM, Metals Park, OH, 1985, p. 2707.
10. J.B. Clark and F.N. Rhines: *J. Met.*, 1957, vol. 209, 425-30.
11. K. Suseelan Nair and M.C. Mittal: *Mater. Sci. Forum*, 1988, vol. 30, pp. 89-103.
12. K.H. Kuo, J.Z. Liang, X.Y. Meng, and Y.K. Wu: *Acta Physica Sinica*, 1982, vol. 31 (7), pp. 988-92.
13. Ya.P. Yarmolyuk, P.I. Kripyakevich, and E.V. Mel'nik: *Sov. Phys. Crystallogr.*, 1975, vol. 20 (3), pp. 329-31.
14. D. Van Dyck, D. Brodelin, J. Mahy, and S. Amelinckx: *Phys. Status Solidi A*, 1987, vol. 103, pp. 357-73.
15. D. Van Dyck, J. Mahy, R. Deblieck, and S. Amelinckx: *Proc. 11th Int. Cong. on Electron Microscopy*, T. Imura, ed., Japanese Society of Electron Microscopy, Tokyo, Kyoto, 1986, pp. 735-36.
16. W.J. Kitchingman and I.M. Vesey: *J. Inst. Met.*, 1970, vol. 98, pp. 52-54.
17. L.Y. Wei and G.L. Dunlop: *New Materials and Processes*, Proc. 5th SSMS, 1989, I.L.H. Hansson and H. Liholt, eds., Danish Society for Materials Testing and Research Ingeniørhuset, Copenhagen, Denmark; Copenhagen, 11 April 1989, pp. 721-28.
18. R.P. Elliott: *Constitution of Binary Alloys*, McGraw-Hill Inc., [by] R.P. Elliott New York, NY, 1965, 1st Suppl., pp. 602-03.
19. J.J. Park and L.L. Wyman: *WADC Tech. Rep.*, 1957, Oct., p. 57-504.
20. R.W. Cahn and P. Haasen: *Physical Metallurgy*, 3rd ed., North-Holland Physics Publishing, Amsterdam, 1983, pp. 240-45.
21. J.M. Cowley: *AIP Conf. Proc. No. 53*, 1979, pp. 1-7.